Physical Mechanisms Providing Clinical Information From Ultrasound Lung Images: Hypotheses and Early Confirmations

M. Demi, R. Prediletto, G. Soldati, and L. Demi

Abstract—In standard B mode imaging, a set of ultrasound pulses is used to reconstruct a 2-D image even though some of the assumptions needed to do this are not fully satisfied. For this reason, ultrasound medical images show numerous artifacts which physicians recognize and evaluate as part of their diagnosis since even one artifact can provide clinical information. Understanding the physical mechanisms at the basis of the formation of an artifact is important to identify the physiopathological state of the biological medium which generated the artifact. Ultrasound lung images are a significant example of this challenge since everything that is represented beyond the thickness of the chest wall (≈ 2 cm) is artifactual information. A convincing physical explanation of the genesis of important ultrasound lung artifacts does not exist yet. Physicians simply base their diagnosis on a correlation observed over the years between the manifestation of some artifacts and the occurrence of particular lung pathologies. In this article, a plausible genesis of some important lung artifacts is suggested.

Index Terms—Lung, medical imaging, ultrasound.

I. INTRODUCTION

AMONG the imaging techniques presently available, ultrasound is a particular and multifaceted technique that offers innumerable advantages. Historically, the extensive application of ultrasound in medicine can be traced back to 1940 [1]. ultrasounds are harmless, they are simple to use, they do not require a specially equipped room as in the case of nuclear magnetic resonance (NMR) or computed tomography (CT), they provide a good temporal resolution, and ultrasound equipment is relatively cheap. A further advantage is that ultrasounds can be effectively used at the bedside, thus causing little or no upset to the patient.

The use of ultrasound in the evaluation of thoracic diseases [2]–[6] is a recent application, and the use of ultrasound as an indication of underlying parenchymal lung disease is even more recent [7], [8]. Today, lung pathologies are mostly diagnosed and monitored by means of chest X-rays and CT scans. Notwithstanding the simplicity, safety, and relatively low cost of ultrasound techniques, ultrasounds are still marginally used because of the high mismatch between the acoustic impedances of air and intercostal tissues. Despite this, it has been evident since 1990s that ultrasound provides important information on pulmonary tissue. When particular lung pathologies are present, ultrasound imaging shows image artifacts, i.e., echographic signs, the interpretation of which is very helpful when dealing with such pathologies. However, the genesis of such signs has not been understood yet and a standard ultrasound imaging technique can only report their presence. Among them, A lines, B lines, and White Lung are three distinct artifacts commonly observed during the examination of the nonconsolidated lungs by ultrasound [9], [10]. A lines (hyperechoic lines also known as horizontal artifacts) are surely the simplest artifacts and are currently explained as evident replicas of the pleural line [11]. On the contrary, B lines (also known as vertical artifacts) and White Lung artifacts are complex signs and a convincing physical explanation of their genesis does not exist yet. Despite the practical role of these artifacts in detecting and monitoring many acute conditions, especially in emergency and critical care settings [12], [13], and despite extensive acoustic characterization studies [14]–[20], their origin is still unclear.

In standard B mode imaging, a set of ultrasound pulses is used to reconstruct a 2-D image even though some of the assumptions needed to do this are not fully satisfied. Just to mention a few: the propagation speed of the acoustic wave is supposed to be constant independently of the propagation medium; the attenuation of the acoustic wave also is supposed to be constant independently of the propagation medium; the size of the beam is assumed to be infinitesimal; refraction is supposed to be absent; and the echoes generated by the acoustic discontinuities of the medium are supposed to reach the probe without any other reflection and to be completely absorbed by the probe. For this reason, ultrasound medical images show numerous artifacts. Clinically, some artifacts are well-known to the physicians [21], [22] who are well aware
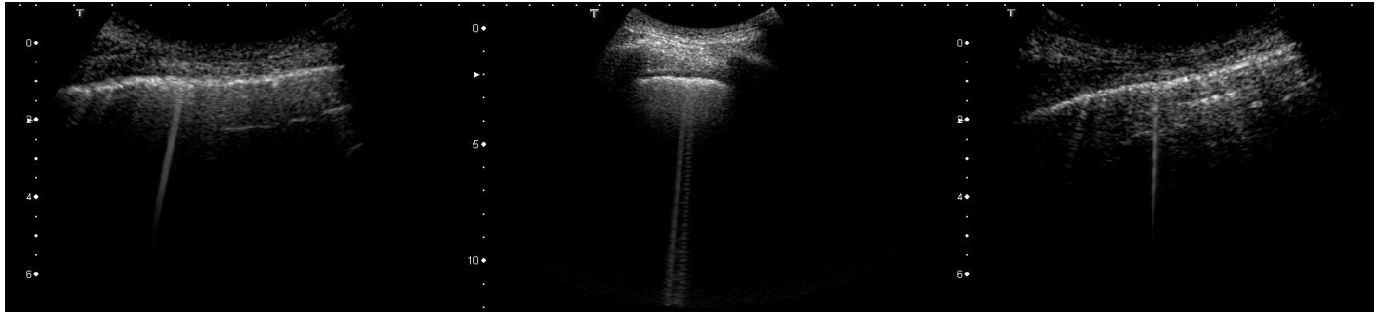
Fig. 1. Left: Example of a nonmodulated B line. Center and Right: Typical examples of modulated B lines which are commonly observed on lung ultrasound images.

that there can be discrepancies between the ultrasound images and the anatomy of the examined medium. Lung images are a significant example of this, and physicians usually evaluate these artifacts as part of their diagnosis since they provide clinical information. An accurate *a priori* knowledge on the genesis of these artifacts is thus indispensable in order to identify the physiopathological state of the lung starting from the visual occurrence of an artifact. In this regard, recent studies showed that the appearance of B lines strongly depends on imaging parameters such as ultrasound pulse bandwidth and carrier frequency. Moreover, these studies indicate that the B lines' native frequencies can be utilized to characterize bubbly structures [23].

In this article, the possible origins of lung ultrasound artifacts, such as B lines and White Lung, are introduced and discussed. Numerous ultrasound image sequences (video clips) were acquired and analyzed on a patient population admitted to the Diagnostic and Interventional Units of our institutes. A Toshiba Aplio XV scanner combined with a PLT-704AT linear probe and a PVT-375BT convex probe was used for imaging. All the ultrasound lung images, which are shown in this article to illustrate the analyzed ultrasound artifacts (except the image in Fig. 6), have been selected from a data set previously acquired by our Respiratory Department during a study which was approved by the local Ethics Committee CEAVNO (study number 1089, approved on January 30, 2017). In this regard, it is necessary to outline that informed consent was requested during the study. A plausible genesis of the B line and White Lung artifacts, which emerged from the analysis of the video clips, is presented and described in Sections III and IV through mathematical models and experimental results.

II. CAN VERTICAL ARTIFACTS BE GENERATED BY VIBRATING AIR BUBBLES?

According to literature, a B line is a modulated narrow bright stripe which starts at the pleura line, goes down to the bottom of the screen, and moves synchronously with lung respiration [24]. Even though a clear definition of the term "modulated" is not provided in medical literature, it is plausible to associate the definition of "modulated stripe" with a vertical stripe including a noticeable periodic structure such as that given by the periodic succession of two different gray levels. It is worth noting, however, that, despite this classification, even nonmodulated B lines are often observed.

In Fig. 1, two examples of modulated B lines and an example of nonmodulated B line, which are commonly observed in lung ultrasound images, are shown.

Moreover, from literature, we know that an air bubble dipped in water vibrates when it is struck by an ultrasound wave and that a vibrating bubble can be a source of ultrasounds [25]. Therefore, the question is: can a vibrating air bubble (in our case, a lung alveolus or an aerated fraction of it in those cases where it has been partially filled by a fluid) generate a B line? To address this question, the simplest mathematical model, which is commonly used to analyze an oscillating (or vibrating) system, is first considered. Let us recall the second-order linear differential equation obtained by equating to zero the sum of the three inertial, dissipative, and elastic forces acting on a mass m in the absence of other external forces

$$F_i + F_d + F_e = 0$$
$$mr'' + dr' + kr = 0. \tag{1}$$

In (1), the mass, the dissipation coefficient, and the elasticity coefficient are indicated by m, d, and k, respectively. With r'', r', and r the acceleration, the velocity, and the displacement of the mass m are indicated, respectively. Obviously, the unknown variable in the previous linear differential equation is the function $r(t)$: that is, the temporal displacement of the mass m (in our specific case $r(t)$ represents the displacement of the wall of an air bubble of radius r dipped in water). The simple second degree characteristic equation must be solved, and the solution $r(t)$ can be written as

$$r(t) = C_1 e^{\alpha_1 t} + C_2 e^{\alpha_2 t} \tag{2}$$

where

$$\alpha_{1,2} = -\frac{d}{2m} \pm \frac{1}{2}\sqrt{\left(\frac{d}{m}\right)^2 - 4\frac{k}{m}} \tag{3}$$

and the constants C_1 and C_2 are determined by the boundary conditions. Let Δ be the radicand in (3), if Δ is either greater or equal to zero, the response of the system is an aperiodic damped motion. The mass m, after an initial displacement induced by a perturbation of its starting position, quickly returns to its starting position without oscillations. Only if $\Delta < 0$, the response of the system is a slightly damped oscillating motion. In this case, the roots α_1 and α_2 are
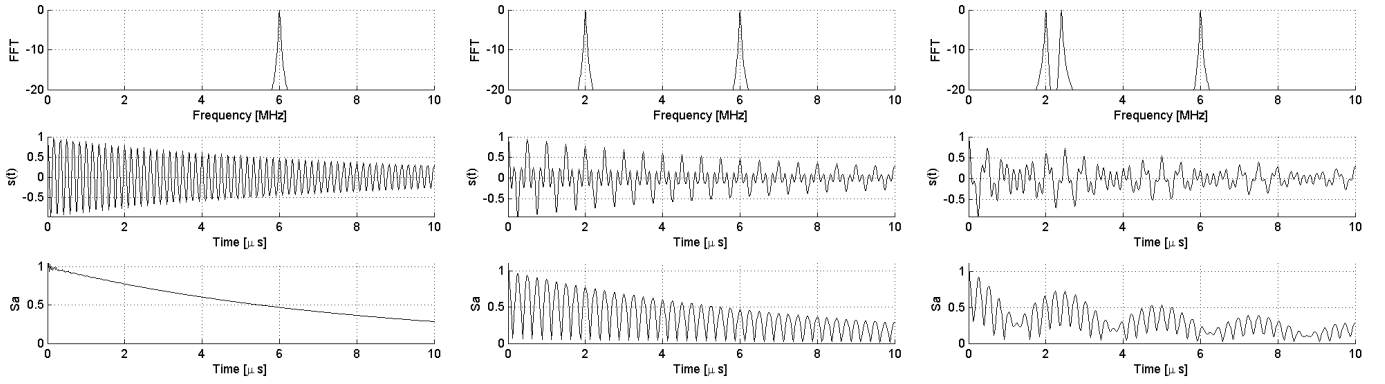
Fig. 2. Left: Plot of a damped harmonic [$s(t)$] of unitary amplitude and frequencies $f = 6$ MHz. Center: Summation $s(t)$ of two damped harmonics of unitary amplitude and frequencies $f_1 = 2$ MHz and $f_2 = 6$ MHz. Right: Obtained $s(t)$ signal if a third unitary harmonic with frequency $f_3 = 2.4$ MHz is added to the two harmonics of 2 and 6 MHz. The power spectra (FFT) and the magnitudes of the analytical signals (S_a) are also shown in the left, right, and center.

complex conjugates and the solution $r(t)$ of the differential equation can be written as

$$r(t) = Ce^{-\frac{t}{\tau}} \cos(\omega_n t + \psi)$$

$$\omega_n = \sqrt{\frac{k}{m} - \frac{d^2}{4m^2}}$$

$$\tau = \frac{2m}{d}. \tag{4}$$

Here again, the constants C and ψ are determined by the boundary conditions. From the analysis of the aforementioned oversimplified dynamic model, we deduce that in order to have a weakly damped vibration from a system like this, once it has been activated by an ultrasound pulse, the radicand Δ must be less than zero, and this happens if the normalized dissipation coefficient is less than 1

$$\frac{d}{2\sqrt{km}} < 1. \tag{5}$$

Let the contribution to the bubble internal pressure by its surface tension be negligible with respect to the hydrostatic pressure in the liquid; let the surrounding liquid be an infinite and incompressible medium; let the radius variation be small with respect to the bubble radius at rest. The values of the three parameters m, k, and d have been estimated [25]–[27] for an air bubble dipped in water as

$$m = 4\pi R_0^3 \rho_L$$

$$k = 12\pi \kappa P_0 R_0$$

$$d = \delta_{\text{tot}} \omega m. \tag{6}$$

The mass m is termed "radiation mass" and represents the water particles which move during the cyclic variation of the bubble radius. The elasticity coefficient k is derived from the air compressibility under the assumption of adiabatic process ($PV^\kappa = $ constant). The dissipation coefficient d is derived from the damping process where the total damping δ_{tot} is given by the sum of the three damping components: the thermal, the reradiating, and the viscous components. In (6), R_0 is the bubble radius at rest, ρ_L is the equilibrium density of the surrounding liquid, κ is the polytropic exponent of the gas,

P_0 is the hydrostatic pressure in the liquid, and ω is the angular frequency of the pulsating bubble. Let ω_n be the angular frequency of the free damped vibration of the air bubble given by (4) and ω_0 be the free vibration of the air bubble in the absence of damping, then the following relationship is obtained from (5) and (6):

$$\frac{1}{2}\delta_{\text{tot}}\frac{\omega_n}{\omega_0} < 1. \tag{7}$$

Since the dimensionless total damping δ_{tot} can be reasonably estimated to be less than 1 for the microbubbles of our interest (aerated spaces of lung with diameter varying between a few microns and 300 μm) [25], then it is easy to verify how (7) holds. However, let us now analyze both the frequency and the damping factor of a pulsating bubble.

Even if (5) is satisfied and, consequently, a damped vibration of the system can be activated by the ultrasound pulse, an artifact similar to a modulated B line cannot be generated yet unless other conditions are satisfied. The acoustic signal provided by (4), once it has been received by the probe, must be transformed into a RF signal $s(t)$ and subsequently the magnitude of the analytical signal $s_a(t)$ [$s_a(t) = s(t) + j s_H(t)$, where $s_H(t)$ is the Hilbert transformation of $s(t)$], must be computed to obtain the gray level function $f(t)$ which ultimately represents a column of the ultrasound image. Let the magnitude of the Fourier transform $F\{\exp(-t/\tau)\}$ of the damping component be null for $|\omega| > \omega_n$, then, according to the properties of the Hilbert transformation, the magnitude of the analytical signal of (4) is precisely given by the damping term and the latter does not provide an oscillating function $f(t)$. That is, a single damped harmonic similar to that of (4) cannot produce the modulated artifacts illustrated in the center and right of Fig. 1 and which have been primarily described in literature [24] as B lines. The left of Fig. 2 shows a damped harmonic [$s(t)$], its power spectrum [fast Fourier transform (FFT)], and the magnitude of the analytical signal (S_a). A single damped harmonic can only give rise to a nonmodulated artifact like the one shown in the left of Fig. 1.

At least two harmonics are needed to obtain a modulated artifact, and the frequency of the two single harmonics must

be compatible with the transfer function of the standard ultrasound probes (convex, linear, or cardiac probes) which are used by physicians to explore the lung. For example, let us suppose a vibrating system gives rise to two harmonics of frequencies $f_1 = 2$ MHz and $f_2 = 6$ MHz of unitary amplitude, then their summation $s(t)$ is equal to the product of two harmonics with frequencies $f_0 = (f_1 + f_2)/2$ and $f_d = (f_1 - f_2)/2$ and the magnitude of the analytical signal $s_a(t)$ is equal to $2|\cos(2\pi f_d t)|$. In this case, the two harmonics of frequencies f_1 and f_2 give rise to a modulated artifact where $f_d = 2$ MHz is the modulation frequency as it is shown in the center of Fig. 2. As an example, the right shows the plot of the magnitude of the analytical signal $s_a(t)$ which is obtained if an *ad hoc* third harmonic with frequency $f_3 = 2.4$ MHz is added to f_1 and f_2. In this case, a low frequency modulation and a high frequency modulation are obtained which could be at the origin of the particular B line observed on the right of Fig. 1.

Hence, as we have seen earlier, a signal $s(t)$ given by the summation of two harmonics with frequencies $f_1 = 6$ MHz and $f_2 = 2$ MHz can provide a modulated artifact such as a modulated B line. However, a different situation occurs if the signal $s(t)$ is given by the summation of two harmonics with frequencies $f_1 = 200$ KHz and $f_2 = 100$ KHz since, in this case, the two frequencies are quite far from the range 1/6 MHz of the medical ultrasound probes. Here, it is worth noting the consequence of this consideration. If the free pulsating frequency f_0 of a bubble in the absence of dissipation is considered and the hypotheses, liquid density ρ_L equal to 10^3 kg/m³, polytropic ratio κ of air equal to 1.4, and hydrostatic pressure P_0 equal to 1 atm, are assumed, then Minnaert's relationship $f_0 \approx 3/R_0$ [Hz] is obtained from (4) and (6). Moreover, from (4), we know that the frequency f_0 in the absence of damping is greater than the frequency $f_n = \omega_n/2\pi$ of the damped vibration. Therefore, given, for example, an air bubble dipped in water with a diameter of 60 μm (a partially deflated alveolus), Minnaert's relationship suggests a resonance frequency $f_n < 100$ KHz. According to Minnaert's relationship, a bubble with a radius less than 3 μm is necessary if it has to radiate a damped acoustic wave with a frequency greater than 1 MHz in water. This is not compatible with the fact that the typical alveolar sac diameter is in the order of hundreds of microns (approximately 280 μm for a healthy lung [28]).

Moreover, besides the problem of frequency, the damping factor τ must be also analyzed. According to literature, a B line starts at the pleura line and goes down to the bottom of the screen ($\approx$4–6 cm). According to the speed of the acoustic wave, a bubble that radiates an ultrasound wave for 80 μs is necessary to generate a 6-cm-long artifact on the lung images. However, from (4) and (6), a damping factor $\tau = 2/\omega\delta_{tot}$ is obtained, which shows how the damping of the harmonics provided by (4) increases if their angular frequency increases. Therefore, multiple high frequencies, which could guarantee artifacts similar to the observed modulated B lines, would give rise to short artifacts. Let δ_{tot} be equal to 0.1, frequencies higher than 1 MHz are affected by damping factors τ smaller than 3 μs. Here again, the expected result conflicts with the

experimental observations of artifacts of up to 6 cm which start at the pleura line and go down to the bottom of the screen. Consequently, according to the aforementioned analysis, even the nonmodulated artifact shown on the left of Fig. 1 cannot be generated by a vibrating microbubble.

Obviously, the vibrational process of an air bubble in water is much more complex. The presence of a shell should be included and a nonlinear model should be used to estimate the temporal variations of the radius of the bubble. For example, the Rayleigh–Plesset equation for a spherical pulsating gas bubble in an incompressible liquid could be considered [25]

$$rr'' + \frac{3}{2}r'^2$$
$$= \frac{1}{\rho_L}\left[P_{G0}\left(\frac{R_0}{r}\right)^{3\kappa} + P_V - \frac{2\sigma}{r} - 4\eta_L\frac{r'}{r} - P_0 - P_{ac}(t) \right]. \tag{8}$$

In (8), P_{G0} is the equilibrium pressure inside the bubble, P_V is the vapor pressure inside the bubble, σ is the surface tension for the liquid–gas interface, η_L is the dynamic viscosity of the liquid, and $P_{ac}(t)$ is the driving acoustic pressure. In this case also, at the end of the perturbation induced by $P_{ac}(t)$, the radius $r(t)$ slowly returns to its equilibrium value R_0 through cyclic oscillations. A temporal function $r(t)$, which is altered with respect to the single damped harmonic provided by (4), is suggested by this equation as a solution to the vibrational process. In this case, due to the nonlinearity, higher order harmonics are also present and the multiple harmonics could generate a modulated vertical artifact. However, independently of the type of shell which can be reasonably included considering the context of a biological medium, the frequency of the fundamental harmonic is probably not too dissimilar from the frequency of the harmonic provided by (4). Consequently, there are two problems that still make the generation of a B line, by the nonlinear vibrational process of an air bubble, unlikely. Given, for example, the previous air bubble of 60 μm with a fundamental frequency of about 100 KHz, then the magnitude of higher order harmonics (e.g., those within the 30th and the 60th order which are compatible with the probe transfer function) should be high enough to provide a good signal-to-noise ratio in order to be detected by the probe. Moreover, the length of the potential artifact would still not be congruent with the length of a B line due to the damping factor which increases with the frequency.

For sake of completeness, shape vibration modes must also be considered beyond the radial mode. Let the bubble surface $r(t,\theta)$ be described as a summation of spherical harmonics of n degree and zero order $Y_n^0(\theta)$

$$r(\theta, t) = R_0 + \sum_{n=0}^{N} A_n(t)Y_n^0(\theta). \tag{9}$$

Let the amplitude $|A_n(t)|$ of the shape variations be much smaller than the radius R_0 of the bubble at rest, then, a valid estimate of the temporal functions $A_n(t)$ can be provided by the solution of a second-order linear differential equation as in the case of the damped oscillator of (1). Given a single uncoated air bubble of radius R_0, dipped in a liquid of
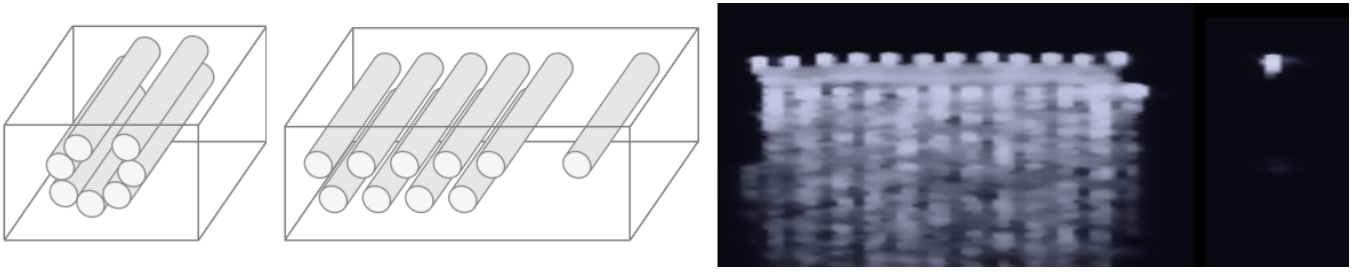
Fig. 3.   Left and Center: Schemes of two phantoms where air cylinders are included in a box of agar solution. Right: Ultrasound image obtained when two layers of 12 superimposed air cylinders and an isolated air cylinder in agar solution are sonified. The two layers of superimposed air cylinders provide long ultrasound artifacts while the isolated air cylinder does not provide artifacts. In this case the 12 superimposed air cylinders had a diameter of 1 mm, interaxial distance equal to 1.5 mm, and a spatial configuration equal to that illustrated in the center.

density ρ_L and viscosity μ, a solution similar to that of (4) is obtained for every function $A_n(t)$ where the angular frequencies and the damping factors assume the following values [29]:

$$\omega_n^2 = (n - 1)(n + 1)(n + 2)\frac{\sigma}{\rho_L R_0^3} \tag{10}$$

$$\frac{1}{\tau_n} = (n + 2)(2n + 1)\frac{\mu}{\rho_L R_0^2}. \tag{11}$$

Let the surface tension σ at 20 °C at sea level and the equilibrium density ρ_L for pure water be 0.072 N/m and 10^3 Kg/m^3, respectively, then in the case of the aforementioned air bubble of 60 μm, according to (10), the frequencies $f_2 = 30$ KHz and $f_6 = 140$ KHz are obtained, for example, for the mode numbers two and six. Moreover, damping increases with the mode number, as shown by (11), and short artifacts would be provided by unlikely shape vibration modes with $n > 10$ ($f_{10} \approx 300$ KHz; $\tau_n \approx 4$ μs). In addition, many periods of a forcing driving frequency are needed to activate a shape vibration mode [30]: that is, long pulses should be used to activate a shape vibration mode while short pulses are usually used in ultrasound medical imaging. To make matters worse, the pulse amplitude, which is needed to activate a shape vibration mode increases as the difference between the central frequency of the driving pulse and the radial resonance frequency of the bubble increases, and, as we have seen, the pulse central frequency (4/6 MHz) is usually much higher than the radial resonance frequency ($\approx$100 KHz for a 60-μm bubble).

There is a lot of evidence to suggest that frequencies greater than 1 MHz cannot be produced by vibrating air bubbles unless their diameter is similar to that of the microbubble contrast agents, which are typically less than 10 μm in diameter. Moreover, the free vibration of a microbubble is not expected to last more than a few microseconds and, consequently, cannot generate an artifact which starts at the pleura line and goes down to the bottom of the screen (4/6 cm).

III. B Lines and Their Structure

The genesis of ultrasound-modulated artifacts similar to B lines has been illustrated on metallic rods and spheres [31]. Phantoms have been also designed with the objective of simulating a distribution of pulmonary alveoli by including airspaces in a tissue-mimicking medium [32]–[35].

Specific phantoms such as those illustrated in the left and center of Fig. 3, where air cylinders simulated a distribution of alveolus and gelatin simulated the tissues of the chest wall, have been introduced and analyzed in [11]. These phantoms provided two important results: 1) the ultrasound artifacts that were observed under isolated metallic rods were not observed below isolated cylinders of air, 2) long ultrasound artifacts were observed when the probe illuminated several air cylinders close to one another (see the right of Fig. 3). The logical conclusion is that air cylinders originate artifacts similar to B lines by means of multiple reflections between them. In other words, a tissue-mimicking area limited by air walls can trap a part of the energy of the incident wave and gradually reradiate it to the probe as a secondary ultrasound source. A conclusion which is also suggested by the experimental results illustrated in other articles such as [32] and [36].

It is worth noting, however, that every B line has its own structure as is illustrated in Fig. 1. A vertical artifact can appear as a sequence of alternating white and black horizontal bands, it can appear as a vertical bright stripe with a constant gray level, and it can be narrow or wide. The spatial distribution of the gray level bands within the vertical artifact can be the expression of a precise periodic function or an aperiodic function. Obviously, a vertical artifact is also affected by tissue generated speckle noise and by the superposition of the replica and mirror effects of the chest wall structures, but this overlapping alone is not sufficient to explain the different structures of the observed B lines. In Fig. 4, examples of artifactual patterns obtained on patients suffering from cardiogenic pulmonary edema, idiopathic pulmonary fibrosis, and acute respiratory distress syndrome (ARDS) are shown. The figure shows how, despite the original definition of bright modulated artifacts, their structure can be even that of a completely random gray level distribution. These particular artifacts will be recalled and discussed at the end of Section IV. In this section, our attention will be focused on the so-called modulated artifacts.

Let us consider a plausible acoustic trap: a small volume of fluid surrounded by aerated alveoli as in the case illustrated in the left of Fig. 3. If an aperture exists, between the surrounding alveoli on the top of the trap at the pleura line, then an ultrasound pulse can enter the trap and be internally reflected by its walls. These multiple reflections, in turn, act as a secondary ultrasound source and part of the trapped energy
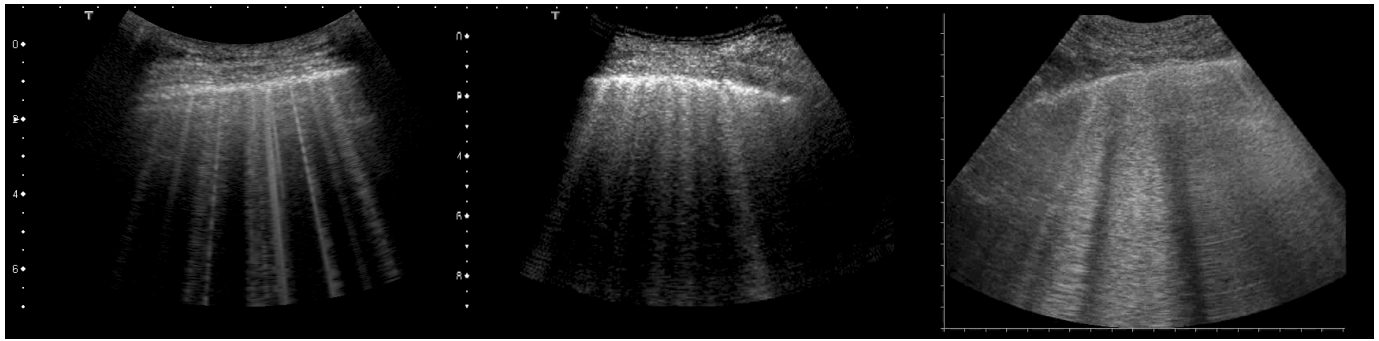
Fig. 4. Left, Center, and Right: Examples of vertical artifacts obtained on patients suffering from cardiogenic pulmonary edema, idiopathic pulmonary fibrosis, and ARDS, respectively.

is reradiated to the probe across the aperture. A similar result can be obtained by means of a simple phantom: a structure A1 dipped in a medium A2 where the structure A1 is delimited by two planar surfaces S and S' and the ultrasound beam is orthogonal to S and S'. Given a pulse $p(t)$, then, once it has been transmitted from the medium A2 to the structure A1, we expect multiple reflections between the two surfaces S and S' and, consequently, an echo $s(t)$ as follows:

$$s(t) = \gamma(t) \sum_{n=-\infty}^{\infty} p(t - n\Delta t) \qquad (12)$$

where $\gamma(t)$ is an attenuation factor for $t \geq 0$ and equal to zero for $t < 0$. Consequently, according to the properties of the Fourier transform

$$S(f) \approx \Gamma(f) * P(f) \sum_{n=-\infty}^{\infty} \delta(f - n\Delta f) \qquad (13)$$

where $\Delta f = 1/\Delta t$. Let us simplify (13) by neglecting the attenuation process due to the introduction of the function $\gamma(t)$ and its Fourier transform $\Gamma(f)$. In this case, because of the periodicity Δt, the power spectrum of the echographic signal $s(t)$ is given by a set of regularly spaced harmonics ($f_n = nc_0/2d$) of the pulse spectrum where the frequency interval Δf is proportional to the ultrasound propagation speed c_0 and inversely proportional to the thickness d. If d is large enough with respect to the pulselength, so that successive pulse reflections are not superimposed, then the vertical artifact generated by the trap is given by the simple repetition of the pulse every Δt seconds. However, if the size of the trap decreases, then the multiple reflections of the pulse give rise to an echo signal where the pulses are no longer separated and the echo power spectrum is characterized by a minor number of harmonics. In the case of a small trap, the power spectrum of the echo signal can even be reduced to a single harmonic and the image formation process can consequently generate an artifact with a constant gray level. According to this model, the length of the vertical artifact depends on the amount of energy transmitted by the pulse to the acoustic trap and on the attenuation factor $\gamma(t)$ which is expected to mainly depend on the nature of the trap internal medium. A poor contribution is expected to be given by the internal reflections to the attenuation factor $\gamma(t)$. This is due to the high acoustic mismatch at the tissue–air interface since this means that the reflection coefficient is close to 1.

Unlike the vibrating bubble, an acoustic trap can generate various modulated artifacts which start at the pleura line and reach the bottom of the screen. Indeed, if the aperture at the top of the trap is sufficiently large with respect to the acoustic beam, then the only limit to the artifact length is given by the attenuation factor $\gamma(t)$. Since the latter cannot be very dissimilar from the attenuation factor of the chest wall, it is logical to expect a signal $s(t)$ having a magnitude similar to the magnitude of the other echo signals generated by the chest wall because of the multiple reflections between the probe and the pleura plane. Let the ultrasound propagation speed be equal to 1540 m/s and the distance between S and S' be equal to d, if a Gaussian pulse with central frequency f_c equal to 6 MHz and duration equal to 1.2 μs is used, then Fig. 5 shows simulated echoes (RF) generated by structure A1 when varying its thickness. The echo power spectra (FFT), the magnitude of the analytical signals (S_a), and the obtained artifacts are also shown. The mathematical model introduced with (12) and its Fourier transformation provides us with a convincing predictor of artifacts similar to those illustrated with the left and center of Fig. 1 and with the left of Fig. 4.

Obviously, in general, the shape of an acoustic trap, given by a small volume of fluid or by any other transonic area surrounded by the alveoli, cannot be described by a single measure as in the case of structure A1. In particular, when the size of the trap increases, a more complex shape is realistic and a more complex spectral signature is expected. For example, if the shape of an acoustic trap could be approximately defined by three dimensions d_1, d_2, and d_3, then its spectral signature would be characterized by the harmonics $f_{n,m,l}$

$$f_{n,m,l} = \frac{c_0}{2}\sqrt{\left(\frac{n}{d_1}\right)^2 + \left(\frac{m}{d_2}\right)^2 + \left(\frac{l}{d_3}\right)^2} \qquad (14)$$

where n, m, and l are integer numbers [37]. Consequently, isolated vertical artifacts with elaborate gray level structures can be observed both on phantoms and on patients. It is worth noting that (14) provides the same spectral signature ($f_n = nc_0/2d$) provided by (12) when two of the three dimensions (d_1, d_2, and d_3) are much greater than the third. As an example, the structure of the artifact, which is illustrated in the right of Fig. 1, can be easily explained with (14) since the latter is the basis of the double modulation illustrated on the
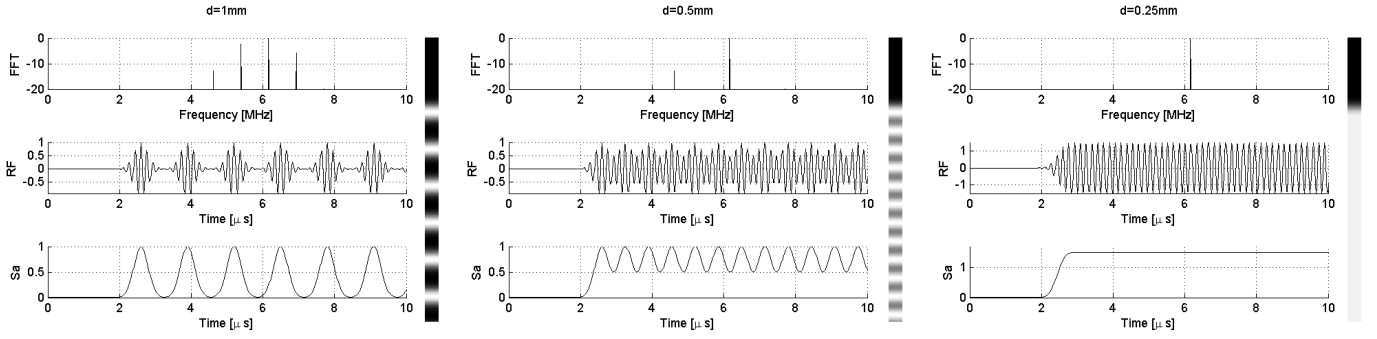
Fig. 5. Simulated echoes (RF) generated by a planar structure orthogonally oriented to the ultrasound beam when varying its thickness d. The echo power spectra (FFT), the magnitude of the analytical signals (S_a), and the obtained artifacts are also shown.

Fig. 6. Appearance of vertical artifacts when varying the central frequency of the pulse from 3 MHz (left) to 6 MHz (right) during the examination of a patient by using a Toshiba Aplio XV scanner combined with a PVT-375BT convex probe.

right of Fig. 2 (here, the native frequencies, $f_{1,0,0} = 2$ MHz, $f_{0,1,0} = 2.4$ MHz, and $f_{0,0,1} = 6$ MHz, and, consequently, the three dimensions, $d_1 = 385$ μ, $d_2 = 321$ μ, and $d_3 = 128$ μ have been simulated). To summarize, the focal point is that, once a transonic area surrounded by aerated spaces has been activated by an ultrasound pulse, it can generate various modulated vertical artifacts similar to the so-called B lines.

From a theoretical point of view, the framework is clear: 1) every acoustic trap has its own spectral signature which depends on the shape, size, and nature of the transonic medium and 2) the ultrasonic pulse is characterized by a frequency band. Consequently, a specific pulse activates specific native frequencies of the acoustic trap and the obtained vertical artifact assumes a consequent visual structure. The results presented in [23] confirm the influence of the pulse bandwidth and its center frequency on the appearance of B lines. As a further example, Fig. 6 shows how vertical artifacts only appeared when the central frequency of the pulse was changed from 3 to 6 MHz during the examination of a patient with the PVT-3758T convex probe.

IV. WHITE LUNG

The artifactual pattern that physicians call White Lung is characterized by a granular and mostly white texture which starts at the pleura line and ends at the bottom of the screen. Two observations, in particular, suggest a plausible genesis of this artifactual pattern: it shows up as a gray level pattern that tends to white and to a granular distribution. The white pattern

recalls the answer of an acoustic trap which is much smaller than the pulselength (an event which has been described in Section III), and the grain-like pattern suggests uncorrelated echoes. The small diameter of the scattering bubbles, their small relative distance, and their random distribution are probably the three conditions which are at the basis of the White Lung artifact. In this case, the ultrasound beam illuminates numerous transonic channels that transmit part of the pulse energy to the underlying acoustic traps. Given the random distribution of the scatterers, uncorrelated echoes are obtained since the ultrasound beams generated by subsequent pulses illuminate areas of the pleura plane with different scatterer distributions. Given a pulse $p(t)$, in this case, we expect an echo signal as follows:

$$s(t) = \gamma(t) \sum_{n=-\infty}^{\infty} \frac{1}{M} \sum_{m=1}^{M} \upsilon p(t - n\Delta t - u) \quad (15)$$

where Δt represents the mean temporal interval between two subsequent reflections transmitted to the probe through every transonic channel; the random variable u introduces the variability of the geometric distribution of the scatterers; the summation with respect to m introduces the contribution of the M transonic channels (penetrated by the ultrasound beam) which add up to form the signal $s(t)$; the normalization factor $1/M$ is necessary since, in this case, the total energy $\gamma(t)$ penetrates the scatterer distribution through M transonic channels; and the random variable υ introduces a variability between the amount of acoustic energy transmitted and subsequently reradiated through every transonic channel at
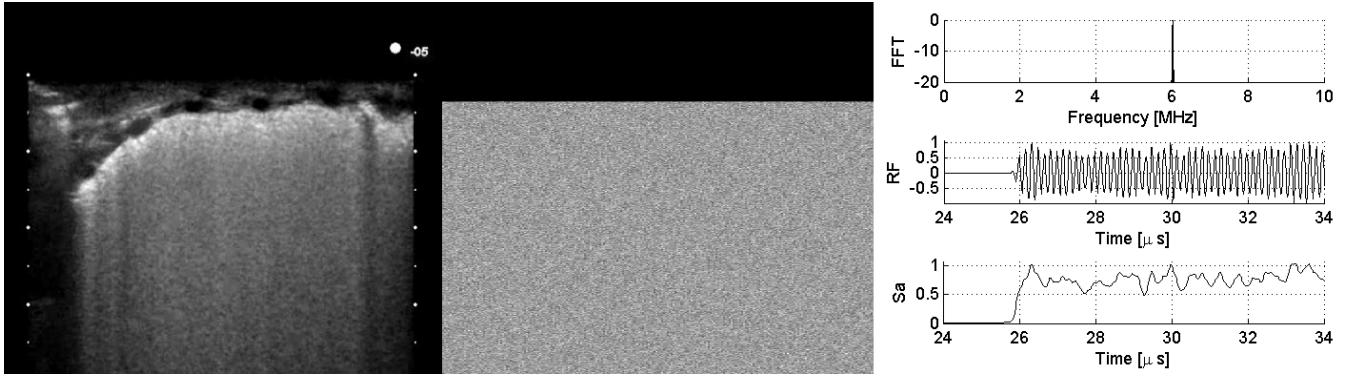
Fig. 7. Left: Typical White Lung artifact. Center and Right: Simulated White Lung artifact and a simulated echo (RF) obtained with (15). The echo power spectrum (FFT) and the magnitude of the analytical signal (S_a) of the echo signal RF are also shown in the right.

every subsequent reflection within the scatterer distribution. The Fourier transform of $s(t)$ can be written as

$$S(f) = \Gamma(f) * \left[P(f) \sum_{n=-\infty}^{\infty} e^{-i2\pi f n \Delta t} \frac{1}{M} \sum_{m=1}^{M} v e^{-i2\pi f u} \right]. \quad (16)$$

Let us assume u and v be two independent random variables. The expected value $E_\xi(f)$ and the variance $\sigma_\xi^2(f)$ of the random variable $\xi(f) = v(\exp(-i2\pi f u))$ can be easily computed. Moreover, the normalized summation $\Sigma_M(\xi)$ of the M random variables $\xi(f)$ in (16) can be seen as a classical estimate of $E_\xi(f)$. Therefore, let M be sufficiently large, so that the variance $\sigma_\xi^2(f)/M$ of the normalized random variable $\Sigma_M(\xi)$ be sufficiently small, then the summation can be replaced by the expected value $E_\xi(f)$ [39, Sec. 8]. Hence, according to the properties of the Fourier transform, the following equation is obtained for the expected value of $S(f)$:

$$E\{S(f)\} = \Gamma(f) * \left[P(f) E_\xi(f) \sum_{n=-\infty}^{\infty} \delta(f - n\Delta f) \right] \quad (17)$$

where $\Delta f = 1/\Delta t$. Here again, let us simplify (17) by neglecting the attenuation process due to the introduction of the function $\gamma(t)$ and its transform $\Gamma(f)$. In this case, the following relationship is obtained:

$$E\{S(f)\} = P(f) E_\xi(f) \sum_{n=-\infty}^{\infty} \delta(f - n\Delta f). \quad (18)$$

As expected, a relationship similar to (13) is obtained because of the assumption of a sufficiently small variance of the random variable $\Sigma_M(\xi)$. Even in this case, the expected frequency spectrum of the echo signal is given by a set of regularly spaced harmonics of the pulse spectrum ($f_n = nc_0/2d_m$) weighted by $E_\xi(f)$ where the frequency interval Δf between two harmonics is proportional to the ultrasound propagation speed c_0 and inversely proportional to the mean distance d_m between contiguous scatterers ($\Delta f = c_0/2d_m$). Consequently, in the case of small values of d_m with respect to the pulselength, when both the frequency interval Δf and the frequency f_1 of the first harmonic increase, the frequency

spectrum $S(f)$ of the echo $s(t)$ can be reduced to a single harmonic of frequency $f_{\Delta t} = 1/\Delta t$ and (15) provides a result very similar to the White Lung artifact. The amplitude of the harmonic (i.e., the white level of the artifact) depends on the magnitude of the frequency component $f_{\Delta t}$ of the pulse spectrum and on the expected value $E_\xi(f)$ computed for $f = f_{\Delta t}$. Multiple reflections between two or more layers of small, close, and randomly distributed scatterers (even though a physiological mean distance between them is expected) give rise to a granular white texture.

The image in the left of Fig. 7 shows a typical White Lung artifact. The image has been selected from an echographic sequence as acquired from a newborn baby with Hyaline membrane disease where the estimated alveolar diameter was 50 μm. Let $d_m = 128$ μm and $c_0 = 1540$ m/s. Let $h_u(u)$ be a uniform probability density function with zero mean value ranging between $-\Delta t/4$ and $\Delta t/4$ and $h_v(v)$ be a uniform probability density function with unitary mean value ranging between 0 and 2 intensity units (i.u). Let the simulated focused beam be large enough so that 25 transonic channels can lie within the focused area ($M = 25$). If a Gaussian pulse with central frequency f_c equal to 6 MHz and pulselength equal to 0.5 μs is used, then a simulated White Lung artifact and a simulated echo (RF) obtained with (15) are shown in the center and right of Fig. 7, respectively. Here, once again, it is worth noting that the pulse power spectrum and the beamwidth play an important role in the artifact formation process. The echo power spectrum (FFT) and the magnitude of the analytical signal (S_a) are also shown in the right of Fig. 7.

It is worth noting that (15) suggests a process where every single reflection inside a distribution of traps is characterized by its own delay and amplitude. In addition to suggesting a physical explanation of the White Lung artifact, (15) suggests a physical explanation also to the local vertical artifacts with a confused structure which are observed for example in patients with pulmonary fibrosis or ARDS. When varying the pulse power spectrum and the values of its parameters M and Δt, (15) provides interesting numerical results similar to the unstructured and to the partially structured vertical artifacts often observed in clinical images.

Obviously, (15) is a basic mathematical model but the numerical results provide images and vertical artifacts very

similar to those provided by the clinical cases of White Lung and fibrosis, respectively. Moreover, it is in line with what has been observed both on patients and on phantoms. On patients [39], the lung ultrasound images show how the artifactual pattern changes by increasing the alveoli internal pressure and, consequently, their size and dominance with respect to the surrounding lung tissue. Analogously, on phantoms [40], ultrasound images show how the artifactual pattern changes by increasing the dominance of the air spaces with respect to water. These articles show how the artifactual pattern changes from White Lung to multiple unstructured vertical artifacts and, subsequently, to isolated modulated B lines by progressively increasing the dominance of the air spaces.

V. Clinical Considerations

An acoustic trap is characterized by one or more transonic access channels and by one or more transonic spaces within which the temporal variation of pressure, which is generated, ultimately acts as a multiple ultrasound source. In pulmonary diseases, in the presence of septal pathologies as in the early stages of cardiogenic pulmonary edema (i.e., interstitial pulmonary edema), transonic access channels to acoustic traps exist and their size is estimated to range between 100 and 300 μm. The edematous interlobular septa, for example, are presumed to have a thickness greater than 150 μm [41], [42]. In ARDS, the inflammatory process irregularly thickens the alveolar walls and the interstitial space, acute fibrinous and organizing pneumonia are the final result. The alveoli are small, and they are layered by a hyaline membrane and show a marked deflation [43]. In this case, a situation of a few collapsed alveoli can give rise to transonic access channels in the order of 200–500 μm. In the case of pulmonary fibrosis, the proliferation of subpleural interstitial tissue can give rise to transonic access channels ranging in size from 200–300 μm to millimeters [44]. The point is that the access channel must allow the penetration of sufficient acoustic energy to generate a visible artifact on the ultrasound images. For example, the LA533 probe from ESAOTE in the focus region has a FWHM between 450 and 700 μm [45] which varies with the imaging parameters. It is, therefore, reasonable that this probe can generate visible vertical artifacts, for example, in correspondence to 300 μm interlobular septa. It should be highlighted, however, that the penetration of sufficient acoustic energy can be guaranteed in two ways: the first is to have an access channel with a size comparable to the lateral and azimuth sizes of the acoustic beam and the second is to use pulses with high power density. It is for this reason that probes characterized by different spatial resolutions and by pulses of different amplitude and duration (e.g., a linear and a convex probe when used with a vascular and an abdomen protocol, respectively) can give rise to different results even if the same pulse central frequency is used. Moreover, the definition of B line found in literature [24] "the B line is a modulated narrow bright stripe which starts at the pleura line, goes down to the bottom of the screen, and ......" must be also reconsidered. Observations on the acquired data set clearly show that the vertical artifacts do not always reach the bottom of the screen and this could be correlated either with the amount of energy that has penetrated the trap or with the attenuation of the transonic medium which characterizes the trap. The possibility of using the artifact length to characterize the material trapped between the air spaces (e.g., water, blood, or tissue) should be investigated since the latter would provide useful clinical information. Moreover, it emerges from the same data set that the visibility of the B lines does not always start at the pleura line. Here, two hypotheses at least should be considered: 1) at the pleura plane the magnitude of the replica and mirror effects can be higher than that of the artifact and the latter can be initially masked by these effects, 2) a complex interaction of the ultrasound pulse with the distribution of the aerated spaces can delay the reradiation of the trapped energy. In addition, the shape of an artifact should be analyzed only between the pleura line and its first replica (the first A line) independently of its length. Beyond the first A line, the shape of the artifact can be modified by a successive acoustic penetration of the trap due to the multiple reflections between the pleura line and the probe.

The generation of an artifact may involve either only one channel, as in the case of an isolated B line, or more channels, as in the case of the White Lung. The latter, for example, is typically observed in Hyaline membrane disease of the newborn and involves small alveoli (about 50 μm) separated by a mean distance in the order of 100–150 μm [46]. In this case, let the beam size in the focus be about 500 μm; it is then possible to hypothesize the activation of about 10 transonic channels. While the size of the transonic channels mostly determines the visibility of the potential artifact, it is the size and the shape of the underlying transonic spaces that determine the structure of the artifact. The B lines with a clear periodic modulation are probably generated by traps that have (or that approximate) a simple geometric shape. Transonic spaces with a complex shape cannot give rise to B lines with a clear periodic modulation. Usually, these artifacts have a confused structure as in the case of pulmonary fibrosis when the interstitial thickening is randomly distributed.

In addition, there is a limit to the size of the acoustic traps under which these cannot be visually detected through a B line. This happens because the lowest native frequency of a trap increases as the size of the trap decreases. Therefore, the native frequencies of a small trap can lie beyond the probe band. A trap of 60 μm, for example, responds with a frequency of 12 MHz (since $f_1 = c_0/2d$) while a trap of 50 μm responds with a frequency of 15 MHz. Not to mention that, as the size of the trap decreases, it is logical to expect a reduction in the size of its access channel. Consequently, the penetration of an insufficient amount of energy does not allow the generation of an artifact with a good signal to noise ratio.

All the ultrasound image sequences acquired on a population of patients suffering from heart failure, *chronic obstructive pulmonary disease* (*COPD*), respiratory insufficiency, *pneumonia*, cardiogenic pulmonary edema, ARDS, and idiopathic pulmonary fibrosis showed artifacts. Nowadays, physicians know that these artifacts are related to the increase of the tissue or liquid components with respect to the air component in the lungs suffering from pulmonary diseases. The variation of the lung superficial

density with the pathology is well documented in medical literature [47], [48], and it is the basis for the existence of transonic channels and acoustic traps below the pleura plane. However, it is worth noting that the characteristics of the artifacts do change depending on the pathology [49], [50].

Cardiogenic pulmonary edema, for example, gives rise to artifacts which are different from those generated by ARDS and idiopathic pulmonary fibrosis since distribution, morphology, size, and content of the acoustic traps change with the pathology. Subjects with cardiogenic pulmonary edema (particularly early cardiogenic pulmonary edema) showed diffuse, brilliant, and thin B lines, often with a periodic internal structure (alternating black and white stripes). Examples of these kinds of B lines appear in Fig. 1 and in the left of Fig. 4. This result did not surprise us since current medical evidence clearly establishes that the distribution of alveoli in the pleural plane in patients with cardiogenic pulmonary edema is characterized by the presence of thickened but anatomically regular interlobular septa which have a similar morphological appearance, a low attenuation capability, and a small width [51]. The width of the interlobular septa exceeds its natural limit (about 500 μm) only in the case of the advanced stages of cardiogenic pulmonary edema when alveolar flooding and alveolus collapse occur. Therefore, both clinical expectations and the experimental results illustrated in Figs.1 and 2 and Figs.4 and 5, respectively, suggest that the B lines observed in the presence of cardiogenic pulmonary edema can be described by means of the two mathematical models (13) and (14).

Conversely, the distribution of alveoli in the pleural plane in patients with idiopathic pulmonary fibrosis is characterized by the presence of larger, irregular, attenuating acoustic traps with small residual airspaces. This is due to the irregular and random proliferation of fibrous tissue at the level of the pulmonary interstitium [52]. Subjects with idiopathic pulmonary fibrosis showed a spatial distribution of B lines as is shown in the center of Fig. 4. B lines did not show a clear periodic structure (even though periodicity was sometime perceivable) and their length and width varied a lot. Similar artifacts can be obtained when local distributions of acoustic traps with irregular shapes are considered. In this case, a mathematical model similar to (15) is in line with both the clinical expectations and the numerical results.

The air space distribution in ARDS is also different from the aforementioned two pathologies. Examples of B lines observed in patients suffering from ARDS are shown in the right of Fig. 4. Here, the subpleural lung is characterized by an irregular edematous thickening of the interstitium, by a reduction of the air spaces in the aerated portions of the lungs, by an edematous obliteration of the alveolar structures, and, in the last phase, by fibrous tissue proliferation [53]. The alveoli distribution is what is expected in a pathology that subverts the interstitium with an irregular and randomly distributed fibrotic content and seems to match the model of the White Lung artifact provided by (15) better than idiopathic pulmonary fibrosis.

VI. DISCUSSION AND CONCLUSION

With regard to microbubbles, probably the most critical point is the main assumption which is at the basis of the equations introduced in Section II: the wavelength λ of the acoustic wave generated in water by a free pulsating microbubble is much greater than its radius R_0 at rest. Such an assumption, which derives from the hypothesis of an incompressible medium, implies that only vibrating air microbubbles with a radius of a few microns can radiate in water acoustic waves with frequencies greater than 1 MHz. However, we must bear in mind that the bubble models introduced in Section II assume ideal conditions for granted which are never met in real situations and that, consequently, there can be discrepancies between the expected and the real results [54].

The two phenomena of vibrating air bubble and vibrating transonic volume are usually illustrated by using two different mathematical models. The former is explained as an oscillating system while the latter is explained through the development of standing waves. Nevertheless, the two models are based on equivalent physical parameters such as radiant mass (medium density), elasticity (compressibility), and damping factor (attenuation). The substantial difference between the two phenomena is the expected frequency of the radiated acoustic wave. Let λ be the wavelength of the radiated acoustic wave and D be either the diameter of an air bubble or the diameter of a transonic volume, the mathematical model of the vibrating air bubble is based on the assumption $\lambda \gg D (f \ll c_0/D)$ while the mathematical model of the transonic volume is based on the assumption of $\lambda \leq 2D (f \geq c_0/2D)$. Given an air bubble with a diameter of 150 μm surrounded by a biological liquid, and a small volume of biological liquid with the same diameter surrounded by air bubbles, then, once they are activated by an ultrasound driving pulse: 1) the pulsating air bubble radiates a 40-KHz fundamental frequency, while the lowest native frequency of the small volume of fluid is 5 MHz. In our opinion, (12), (14), and (15) provide a plausible physical explanation of numerous artifacts commonly observed on pulmonary ultrasound images even though other mechanisms cannot be excluded. The air space distributions in the lung depend on the pathology and in the case of particular air space distributions, artifacts may be generated which cannot be explained with the above mechanisms. However, given a vertical artifact which extends from the pleura plane to the bottom of the screen and moves with the pleura sliding, our suggestion is to look for a logical explanation to the structure of the artifact primarily through reflections between air spaces separated by a transonic medium

The spectral analysis of the vertical artifacts observed on the patient data set is not provided in this article since this data set was acquired by means of a medical ultrasound scanner (Toshiba Aplio XV) which did not allow the storing of the RF signals and, consequently, their subsequent analysis. The next step will be to focus on validating the presented models and hypotheses by analyzing ultrasound RF signals as obtained from clinical data. To do that, a research-dedicated ultrasound scanner, which provides quality diagnostic images, is needed.

Finally, despite being mentioned in the conclusion section, it is important to outline how the debate on the claimed safety of ultrasound exams is still open. The risks of unwanted ultrasound bioeffects are mostly associated with the development of transient cavitation. Rapid pressure variations generate gas pockets in a fluid where the pressure assumes relatively low values and the gas pockets, once they are subjected to high values of pressure, can collapse, giving rise to shock waves. In particular, the inception of transient (or inertial) cavitation in a fluid is facilitated by the presence of gas bubbles as, for example, microbubble contrast agents. Therefore, the lung is an organ where the inception of transient cavitation cannot be neglected because of the presence of aerated spaces. The induction of pulmonary hemorrhage in lung mice by transient cavitation generated by pulsed ultrasound was discovered 30 years ago [55] and a confirmation of the lower threshold for bioeffects in the lung, as compared with other tissues that do not contain gas pockets can be found in [56]. It was subsequently demonstrated that the threshold, beyond which cavitation occurs in the lung, depends on more than two parameters and a modified form of the mechanical index (MI) was proposed for ultrasound pulmonary exams [57]. The article is based on data collected by 14 studies of lung hemorrhage in four laboratory animals (e.g., mouse, rat, rabbit, and pig). Here, a modified MI is proposed where, in addition to the peak value of pressure rarefaction and to the pulse central frequency, the pulse repetition frequency (PRF) and pulse duration (PD) are involved. However, there has been no report of damage to adult or neonatal human lungs so far [58] and, among the ultrasound exams (B mode, M mode, and Color Doppler imaging, and velocity measures by pulsed Doppler) B mode imaging shows the highest safety threshold [59]. Therefore, according to the present knowledge, pulmonary B mode imaging can be securely performed even though the inception of adverse bioeffects cannot be neglected and, consequently, lower values of MI must be used to reduce the risk in potentially vulnerable patients.

ACKNOWLEDGMENT

REFERENCES

[1] K. F. Graff, "A history of ultrasonics," in *Physical Acoustics*, vol. 15. New York, NY, USA: Academic, 1981.

[2] S. Beckh, PL. Bölcskei, and KD. Lessnau, "Real-time chest ultrasonography: A comprehensive review for the pulmonologist," *Chest*, vol. 122, no. 5, pp. 1759–1773, 2002.

[3] S. J. Koenig, M. Narasimhan, and P. H. Mayo, "Thoracic ultrasonography for the pulmonary specialist," *Chest*, vol. 40, no. 5, pp. 1332–1341, 2011.

[4] C. F. Koegelenberg, F. V. Groote-Bidlingmaier, and C. T. Bolliger, "Transthoracic ultrasonography for the respiratory physician," *Respiration*, vol. 84, no. 4, pp. 337–350, 2012.

[5] A. Zanforlin, "The role of chest ultrasonography in the management of respiratory diseases: Document I," *Multidisciplinary Respirat. Med.*, vol. 8, no. 1, p. 54, Aug. 2013.

[6] A. Smargiassi, "The role of chest ultrasonography in the management of respiratory diseases: Document II," *Multidisciplinary Respirat. Med.*, vol. 8, no. 1, p. 55, 2013.

[7] E. Picano and P. A. Pellikka, "Ultrasound of extravascular lung water: A new standard for pulmonary congestion," *Eur. Heart J.*, vol. 37, no. 27, pp. 2097–2104, 2016.

[8] S. H. Rambhia, C. A. D'Agostino, A. Noor, R. Villani, J. J. Naidich, and J. S. Pellerito, "Thoracic ultrasound: Technique, applications, and interpretation," *Current Problems Diagnostics Radiol.*, vol. 46, no. 4, pp. 305–316, 2017.

[9] D. Lichtenstein and G. Mezière, "A lung ultrasound sign allowing bedside distinction between pulmonary edema and COPD: The comet-tail artifact," *Intensive Care Med.*, vol. 24, no. 12, pp. 1331–1334, 1998.

[10] D. A. Lichtenstein, G. A. Mezière, J. F. Lagoueyte, P. Biderman, I. Goldstein, and A. Gepner, "A-lines and b-lines lung ultrasound as a bedside tool for predicting pulmonary artery occlusion pressure in the critically ill," *Chest*, vol. 136, no. 4, pp. 1014–1020, 2009.

[11] M. Demi, G. Soldati, and L. Demi, "On the artefactual information of ultrasound lung images: A lines and B lines," in *Proc. Meetings Acoust.*, 2018, vol. 35, no. 1, Art. no. 020003, doi: 10.1121/2.0000943.

[12] G. Soldati and S. Sher, "Bedside lung ultrasound in critical care practice," *Minerva Anestesiolog.*, vol. 75, no. 9, pp. 509–517, 2009.

[13] F. Corradi, C. Brusasco, and P. Pelosi, "Chest ultrasound in acute respiratory distress syndrome," *Current Opinion Crit. Care*, vol. 20, no. 1, pp. 98–103, 2014.

[14] F. Dunn and W. J. Fry, "Ultrasonic absorption and reflection by lung tissue," *Phys. Med. Biol.*, vol. 5, no. 4, pp. 401–410, 1961.

[15] T. J. Bauld and H. P. Schwan, "Attenuation and reflection of ultrasound in canine lung tissue," *J. Acoust. Soc. Amer.*, vol. 56, no. 5, pp. 1630–1637, 1974.

[16] P. C. Pedersen and H. S. Ozcan, "Ultrasound properties of lung tissue and their Measurements," *Ultrasound Med. Biol.*, vol. 12, no. 6, pp. 483–499, 1986.

[17] F. Dunn, "Attenuation and speed of ultrasound in lung: Dependence upon frequency and inflation," *J. Acoust. Soc. Amer.*, vol. 80, no. 4, pp. 1248–1250, 1986.

[18] F. Dunn, "Attenuation and speed of ultrasound in lung," *J. Acoust. Soc. Amer.*, vol. 56, no. 5, pp. 1638–1639, 1974.

[19] Z. Mikhak and P. C. Pedersen, "Acoustic attenuation properties of the lung: An open question," *Ultrasound Med. Biol.*, vol. 28, no. 9, pp. 1209–1216, 2002.

[20] K. Mohanty, J. Blackwell, T. Egan, and M. Muller, "Characterization of the lung parenchyma using ultrasound multiple scattering," *Ultrasound Med. Biol.*, vol. 43, no. 5, pp. 993–1003, 2017.

[21] J. T. Bushberg, J. A. Seibert, E. M. Leidholdt, Jr., and J. M. Boone, *The Essential Physics of Medical Imaging*. Philadelphia, PA, USA: Williams & Wilkins, 2002.

[22] M. Demi, "The basics of ultrasound," in *Comprehensive Biomedical Physics*, vol. 2, A. Brahme, Ed. Amsterdam, The Netherlands: Elsevier, 2014, pp. 297–322.

[23] L. Demi, W. van Hoeve, R. J. G. van Sloun, G. Soldati, and M. Demi, "Determination of a potential quantitative measure of the state of the lung using lung ultrasound spectroscopy," *Sci. Rep.*, vol. 7, no. 1, 2017, Art. no. 12746.

[24] G. Volpicelli *et al.*, "International evidence-based recommendations for point-of-care lung ultrasound," *Intensive Care Med.*, vol. 38, no. 4, pp. 577–591, 2012.

[25] T. G. Leighton, *The Acoustic Bubble*. Cambridge, MA, USA: Academic, 1994.

[26] H. Medwin, "Counting bubbles acoustically: A review," *Ultrasonics*, vol. 15, no. 1, pp. 7–13, 1977, doi: 10.1016/0041-624X(77)90005-1.

[27] N. de Jong, M. Emmer, A. van Wamel, and M. Versluis, "Ultrasonic characterization of ultrasound contrast agents," Med. Biol. Eng. Comput., vol. 47, no. 8, pp. 861–873, 2009, doi: 10.1007/s11517-009-0497-1.

[28] K. B. Sagar, T. L. Rhyne, G. S. Myers, and R. S. Lees, "Characterization of normal and abnormal pulmonary surface by reflected ultrasound," *Chest*, vol. 74, no. 1, pp. 29–33, 1978.

[29] R. Nabergoj and A. Francescutto, "On the thresholds for surface waves on resonant bubbles," *J. Phys. Colloques*, vol. 40, no. C8, pp. C8-306–C8-309, 1979, doi: 10.1051/jphyscol:1979854.

[30] M. Versluis *et al.*, "Microbubble shape oscillations excited through ultrasonic parametric driving," *Phys. Rev. E, Stat. Phys. Plasmas Fluids Relat. Interdisc. Top.*, vol. 82, no. 2, 2010, Art. no. 026321, doi: 10.1103/PhysRevE.82.026321.

[31] J. J. Faran, "Sound scattering by solid cylinders and spheres," *J. Acoust. Soc. Amer.*, vol. 23, no. 4, p. 405, 1951.

[32] G. Soldati, R. Copetti, and S. Sher, "Sonographic interstitial syndrome: The sound of lung water," *J. Ultrasound Med.*, vol. 28, no. 2, pp. 163–174, 2009.

[33] A. Spinelli *et al.*, "Realization of a poro-elastic ultrasound replica of pulmonary tissue," *Biomatter*, vol. 2, no. 1, pp. 37–42, 2012.

[34] C. Blüthgen, S. Sanabria, T. Frauenfelder, V. Klingmüller, and M. Rominger, "Economical sponge phantom for teaching, understanding, and researching a- and b-line reverberation artifacts in lung ultrasound," *J. Ultrasound. Med.*, vol. 36, no. 10, pp. 2133–2142, 2017.

[35] H. H. Do and S. Lee, "A low-cost training phantom for lung ultrasonography," *Chest*, vol. 150, no. 6, pp. 1417–1419, 2016.

[36] T. Kameda, N. Kamiyama, H. Kobayashi, Y. Kanayama, and N. Taniguchi, "Ultrasonic b-line-like artifact generated with simple experimental models provide clues to solve key issues in B-lines," *Ultrasound Med. Biol.*, vol. 45, no. 7, pp. 1617–1626, 2019.

[37] L. L. Beranek, *Acoustics*. New York, NY, USA: Acoustical Society of America, 1993.

[38] A. Papoulis, *Probability, Random Variables, and Stochastic Process*. New York, NY, USA: McGraw-Hill, 1965.

[39] B. Bouhemad, H. Brisson, M. Le Guen, C. M. B. Arbelot, Q. Lu, and J.-J. Rouby, "Bedside ultrasound assessment of positive end-expiratory pressure-induced lung recruitment," *Amer. J. Respirat. Crit. Care Med.*, vol. 183, no. 3, pp. 341–347, 2011.

[40] G. Soldati, V. Giunta, S. Sher, F. Melosi, and C. Dini, "'Synthetic' comets: A new look at lung sonography," *Ultrasound Med. Biol.*, vol. 37, no. 11, pp. 1762–1770, 2011.

[41] E. N. Milne, M. Pistolesi, M. Miniati, and C. Giuntini, "The radiologic distinction of cardiogenic and noncardiogenic edema," *Amer. J. Roentgenol.*, vol. 144, no. 5, pp. 879–894, 1985.

[42] N. C. Staub, H. Nagano, and M. L. Pearce, "Pulmonary edema in dogs, especially the sequence of fluid accumulation in lungs," *J. Appl. Physiol.*, vol. 22, no. 2, pp. 227–240, 1967.

[43] M. B. Beasley, "The pathologist's approach to acute lung injury," *Arch. Pathol. Lab. Med.*, vol. 134, no. 5, pp. 719–727, 2010.

[44] C. Mai, "Thin-section CT features of idiopathic pulmonary fibrosis correlated with micro-ct and histologic analysis," *Radiology*, vol. 283, no. 1, pp. 252–263, 2017.

[45] L. Demi, J. Viti, L. Kusters, F. Guidi, P. Tortoli, and M. Mischi, "Implementation of parallel transmit beamforming using orthogonal frequency division multiplexing-achievable resolution and interbeam interference," *IEEE Trans. Ultrason., Ferroelectr., Freq. Control*, vol. 60, no. 11, pp. 2310–2320, Nov. 2013.

[46] R. Copetti, L. Cattarossi, F. Macagno, M. Violino, and R. Furlan, "Lung ultrasound in respiratory distress syndrome: A useful tool for early diagnosis," *Neonatology*, vol. 94, no. 1, pp. 52–59, 2008.

[47] G. Soldati *et al.*, "*Ex vivo* lung sonography: Morphologic-ultrasound relationship," *Ultrasound Med. Biol.*, vol. 38, no. 7, pp. 1169–1179, 2012.

[48] G. Soldati, "Lung ultrasonography May provide an indirect estimation of lung porosity and airspace geometry," *Respiration*, vol. 88, no. 6, pp. 458–468, 2014.

[49] G. Soldati and M. Demi, "The use of lung ultrasound images for the differential diagnosis of pulmonary and cardiac interstitial pathology," *J. Ultrasound*, vol. 20, no. 2, pp. 91–96, 2017.

[50] R. Copetti, G. Soldati, and P. Copetti, "Chest sonography: A useful tool to differentiate acute cardiogenic pulmonary edema from acute respiratory distress syndrome," *Cardiovascular Ultrasound*, vol. 6, no. 1, p. 16, 2008.

[51] G. Soldati, M. Demi, A. Smargiassi, R. Inchingolo, and L. Demi, "The role of ultrasound lung artifacts in the diagnosis of respiratory diseases," *Expert Rev. Respirat. Med.*, vol. 13, no. 2, pp. 163–172, 2019.

[52] P. J. Wolters, "Time for a change: Is idiopathic pulmonary fibrosis still idiopathic and only fibrotic?" *Lancet Respir. Med.*, vol. 6, no. 2, pp. 154–160, 2018.

[53] E. T. Obadina, J. M. Torrealba, and J. P. Kanne, "Acute pulmonary injury: High-resolution CT and histopathological spectrum," *Brit. J. Radiol.*, vol. 86, no. 10247, 2013, Art. no. 20120614.

[54] K. Vokurka, "Comparison of Rayleigh's, Herring's, and Gilmore's models of gas bubbles," *Acta Acustica United Acustica*, vol. 59, no. 3, pp. 214–219, 1986.

[55] S. Z. Child, C. L. Hartman, L. A. Schery, and E. L. Carstensen, "Lung damage from exposure to pulsed ultrasound," *Ultrasound Med. Biol.*, vol. 16, no. 8, pp. 817–825, 1990.

[56] L. A. Frizzell, E. Chen, and C. Lee, "Effects of pulsed ultrasound on the mouse neonate: Hind limb paralysis and lung hemorrhage," *Ultrasound Med. Biol.*, vol. 20, no. 1, pp. 53–63, 1994.

[57] C. C. Church and W. D. O'Brien, "Evaluation of the threshold for lung hemorrhage by diagnostic ultrasound and a proposed new safety index," *Ultrasound Med. Biol.*, vol. 33, no. 5, pp. 810–818, 2007.

[58] Z. Izadifar, P. Babyn, and D. Chapman, "Mechanical and biological effects of ultrasound: A review of present knowledge," *Ultrasound Med. Biol.*, vol. 43, no. 6, pp. 1085–1104, 2017.

[59] D. L. Miller, Z. Dong, C. Dou, and K. Raghavendran, "Pulmonary capillary hemorrhage induced by different imaging modes of diagnostic ultrasound," *Ultrasound Med. Biol.*, vol. 44, no. 5, pp. 1012–1021, 2018.